



Molecular engineering of donor-acceptor structured g-C₃N₄ for superior photocatalytic oxytetracycline degradation

Chen Zhang^{a,*}, Zenglin Ouyang^a, Yang Yang^b, Xia Long^c, Lei Qin^a, Wenjun Wang^a, Yin Zhou^a, Deyu Qin^a, Fanzhi Qin^a, Cui Lai^{a,*}

^a College of Environmental Science and Engineering, Hunan University and Key Laboratory of Environmental Biology and Pollution Control, Ministry of Education (Hunan University), Changsha 410082, PR China

^b Department of Chemical and Materials Engineering, University of Alberta, Edmonton, Alberta T6G 1H9, Canada

^c Aerospace Kaitian Environmental Technology Co., Ltd., Hunan, Changsha 410100, PR China

ARTICLE INFO

Keywords:

Photocatalysis
Copolymerization
Donor-acceptor structure
Molecular engineering
Antibiotic degradation

ABSTRACT

The inherent structural defects of graphitic carbon nitride (g-C₃N₄), especially low separation efficiency of photogenerated carriers, have greatly limits its photocatalytic degradation ability towards pollutants. Conjugated g-C₃N₄ (CN) with tailored donor-acceptor units have recently attracted great attention because of the controlled optical bandgap and favorable separation of charge carriers. Here, a novel 5-bromo-2-thiophenecarboxaldehyde (BTC) grafted CN photocatalyst (TCN) was prepared. The results have showed that this new material has significant performance advantages. Up to 2.43-fold apparent rate constant improvement in photocatalytic OTC degradation was realized using TCN-5 compared to CN, and the efficiency for OTC degradation was as high as 93%. And at the end of the reaction (at 60 min), the removal efficiency of TOC was 38%, which should be due to the accelerated the intramolecular charge separation and controllable electron migration. This work unravels intramolecular charge transfer in donor-acceptor structured CN for oxytetracycline photocatalytic degradation, which is expected to bring a promising approach for the photocatalytic degradation of antibiotics.

1. Introduction

With the rapid development of the industrial and urban development, increasing emphasis has been put on environmental pollution and energy shortage [1-4]. Antibiotic contamination has caused an extensive attention due to its threats towards environment [5-9]. As one of the typical antibiotics, oxytetracycline hydrochloride (OTC) has been used to prevent infection widely due to its low cost and broad-spectrum activity. Because of its complex molecular structure, high stability, and low biodegradability, it is urgent to reduce its environmental hazards. There have been numerous studies on eliminating the antibiotic pollutants in water including physical methods, biodegradation methods, and chemical methods. However, the physical methods are not satisfactory, the biodegradation methods take a long time for pollution removal, and the conventional chemical oxidation method may cause secondary pollution [10]. Recently, photocatalysis has become a promising advanced technology for removal of antibiotics in water because of its energy conservation, low cost and high efficiency [11].

Polymeric carbon nitride was first reported in the field of

photocatalysis in 2009 [12]. It has been widely used in photocatalysis, such as CO₂ reduction, H₂ evolution and synthetic organic chemistry because of its chemical stability and environmental benignity [13-16]. However, pristine CN still has many defects such as inadequate optical absorption, fast charge recombination and lack of active sites, which lead to limited photocatalytic activity. Because of its intrinsic conjugated electronic system, the charge separation in CN is uncontrolled, so higher photogenerated carrier recombination rate will be resulted [17]. Thus, there have been a lot of efforts to enhance the separation efficiency between photogenerated electrons and holes such as loading quantum dots for better light sensitization, constructing heterojunction, doping elements, modulating morphology, etc. [16,18-21]. Because conventional strategies may still suffer from limits, it is still a research hotspot to sustainably develop new strategies to improve the photo-generated carrier separation. Construction of donor-acceptor (D-A) configuration can induce internal electric field, which will promote the generation of free holes and electrons [22-24]. The difference brought by electron affinity would strengthen the intramolecular charge transfer, which could drive the electrons on the donor units to the acceptor units

* Corresponding authors.

E-mail addresses: zhangchen@hnu.edu.cn (C. Zhang), laicui@hnu.edu.cn (C. Lai).

<https://doi.org/10.1016/j.cej.2022.137370>

Received 19 March 2022; Received in revised form 20 May 2022; Accepted 1 June 2022

Available online 6 June 2022

1385-8947/© 2022 Elsevier B.V. All rights reserved.

[25]. Consequently, the holes and electrons are separated on the donor units and the acceptor units efficiently, which promote the separation of photogenerated carriers.

In the past few years, many studies have investigated on how to construct CN-based D-A structure. Zhu et al. [25] synthesized several kinds of D-A structured CN photocatalysts via introducing 2-aminobenzothiazole into the CN framework. In our team, Zhou et al. [26] induced 2,5-dibromopyrazine into polymeric carbon nitride (PCN) to obtain an obvious distorted structure. The photocatalyzed degradation rate of sulfamethazine by optimized pyrazine doped PCN was four times higher than that of urea-based PCN. Yang et al. [27] successfully incorporated 2-hydroxy-4,6-dimethylpyrimidine into the CN network by in situ keto-enol cyclization method. The TCN photocatalysts exhibited excellent photocatalytic OTC degradation effect and H₂O₂ production attributing to the expansion of light absorption range and boosted charge separation. In these mentioned cases, acceptor units were introduced into the CN structure. These introduced electron acceptors will promote the efficient separation of the photogenerated electrons and holes in CN. The free radicals that play important role in the photocatalytic degradation process mainly come from the reduction of electrons on the LUMO of CN. The introduction of electron acceptors will cause the decrease of CN LUMO energy, which is not conducive to the production of active species. If an electron donor structure is introduced into the CN framework, it will facilitate the degradation process because the excited electrons are continuously transferred to the CN structure, which can not only promote the separation of photogenerated carriers, but also maintain the reduction potential of CN.

In this work, a novel D-A type CN was synthesized by thermal copolymerization of urea and BTC. BTC is selected because of electron-rich property of the thiophene group and the electron-withdrawing property of the Br atom [28-30]. The thiophene group was induced into the D-A structured CN (TCN-X) successfully. The morphologies, structures, photoelectrochemical and optical properties of the prepared photocatalysts are detailly characterized and analyzed. Then, time-resolved photoluminescence (TRPL) spectra and photoluminescence (PL) spectra are adopted to investigate the photogenerated charges separation dynamics. The doping of BTC can enhance the visible light absorption ability of CN and improve the separation and transfer of photogenerated electrons and holes. Finally, we evaluated the photocatalytic performances of the photocatalysts and discussed the mechanisms and process of OTC degradation. This research may open a new sight on designing highly efficient CN-based D-A structure photocatalysts.

2. Methods and experiments

2.1. Synthesis of CN and TCN

In a typical photocatalyst preparation procedure, a certain volume of BTC and 10 g of urea were mixed. Subsequently, we placed the obtained mixture in an alumina crucible and heated to 550 °C for 2 h with a heating rate of 5 °C·min⁻¹. The resulting products were washed with absolute ethanol and deionized water alternately and dried at 60 °C for 8 h then cooling to room temperature. The volumes of BTC mixed with urea are 1 μL, 5 μL and 10 μL, and the prepared samples were named as TCN-X (X = 1, 5, 10). The pristine CN was produced without adding BTC. For the purpose of better investing solid-state ¹³C nuclear magnetic resonance (NMR), the volume dose of BTC was increased to 300 μL (ACN-300).

2.2. Characterization and analysis

The X-ray diffraction (XRD) information of the prepared photocatalysts were determined by Bruker D8 Focus diffractometer with Cu Kα radiation. X-ray photoelectron spectroscopy (XPS) spectra were performed using a Escalab Xi+ spectrometer with Al Kα as the line

source. The morphologies of the products were obtained on a Zeiss Gemini 300 scanning electron microscope (SEM). A FEI Tecnai G2 F20 S-TWIN electron microscope was adopted to get transmission electron microscopy (TEM) images. UV–vis diffuse reflectance spectra (UV–vis DRS) were collected using a Varian Cary 300 device (BaSO₄ as reference material). TRPL decay spectra were obtained from a FLS 980 fluorescence lifetime spectrophotometer. PL spectra were gained from a PerkinElmer LS-55 fluorescence spectrophotometer. Barrett-Joyner-Halenda (BJH) and Brunauer-Emmett-Teller (BET) methods were analyzed by a nitrogen adsorption analyzer. A total organic carbon (TOC) analyzer was applied to obtain the TOC data. Solid-state ¹³C NMR spectra were acquired from a Bruker Avance III 600 instrument. A Horiba Jobin Yvon LabRAM HR800 Raman spectrometer was used to get the Raman spectra data. Attenuated total reflectance Fourier-transform infrared (ATR-FTIR) were measured through a Thermo Nicolet 5700 spectrophotometer.

2.3. Photoelectrochemical tests

The Mott-Schottky plots, electrochemical impedance spectroscopy (EIS) and transient photocurrent density of the materials were measured by electrochemical workstation (Chenhua CHI 760E). The products were placed in 0.2 mol·L⁻¹ Na₂SO₄ electrolyte with the sample electrode as working electrode, the Pt wire electrode as counter electrode and the Ag/AgCl electrode as reference electrode, respectively. The work electrode preparation was listed as the following: several fluorine-doped tin oxide (FTO) glasses were cleaned by acetone, ethanol, and deionized water sequentially using ultrasonication method. Then, 5 mg of the prepared photocatalysts were mixed with 1 mL 10 % nafion solution with ethanol diluted for slurry production. Finally, the 100 μL of the mixture was dropped on glasses uniformly and dried for 2 h at 120 °C. The simulated light source was acquired from a xenon lamp (PLSSXE300/300 UV, 300 W equipped with a 420 nm cutoff filter).

2.4. Photocatalytic activity tests

The degradation capability of photocatalysts were evaluated by calculating the degradation rate of OTC under visible light irradiation. A 300 W xenon lamp fitted with a glass filter that remove light below 420 nm was provided as the light source. Generally, the 50 mg of catalyst sample was dispersed into 100 mL OTC solution (20 mg·L⁻¹). Before each light reaction, the mixed suspension was continuously stirred under dark conditions for half an hour for the purpose of adsorption–desorption equilibrium. During an hour of light reaction, 3 mL suspension was taken out from the mixture at intervals of 15 min, then filtered to remove the material particles (0.22 μm Millipore filter), and measured by using high-performance liquid chromatography (HPLC, Agilent 1260, USA). The instrument was assembled with a C18 reverse-phase column at 25 °C and a UV–vis detector with 353 nm detection wavelength. The volume of water in the mobile phase was 80%, the volume of acetonitrile was 20%, and 0.1% of HCOOH was added to the mobile phase. The injection volume was 20 μL and the mobile phase flow rate was chosen at 0.1 mL·min⁻¹.

The degradation efficiency (DE, %) of the prepared catalysts was obtained by the equation (Eq. (1)):

$$DE(\%) = \frac{C_0 - C_t}{C_0} * 100\% \quad (1)$$

At the same time, the quasi first-order kinetics of compound fitting of pollutant removal process can be calculated by the following formula (Eq. (2)):

$$\ln C_t / C_0 = -k_1 t \quad (2)$$

where C_t represents the OTC concentration after the t time reaction and C₀ is the initial concentration of OTC solution, k₁ (min⁻¹) presents the

rate constant. The toxicity estimation software tool (T.E.S.T) was used to predict the toxicity of OTC molecule and its degradation intermediates [31].

The TOC measurement was carried out on a TOC analyzer (Shimadzu TOC-VCPH). Moreover, in order to estimate the stability of the catalyst, the catalyst after the reaction was filtered, washed with ethanol and ultrapure water, recovered, and then be dried in drying oven. The process of cyclic experiment was the same as that of photocatalytic degradation.

The contribution of reactive species produced in photocatalytic reaction process was evaluated by the radical trapping experiments. Ethylenediaminetetraacetic acid disodium (EDTA-2Na), 4-hydroxy-2,2,6,6-tetramethylpiperidinyloxy (TEMPOL) and isopropanol (IPA) which were regarded as quencher of holes (h^+), hydroxyl radicals ($\cdot\text{OH}$) and superoxide radical ($\cdot\text{O}_2^-$).

2.5. Degradation path analysis and toxicity assessment tests

The photodegradation reaction intermediates of OTC were determined via liquid chromatography technology coupled with tandem mass spectrometry (LC-MS/MS). The detailed steps can be found in Text S1. The toxicity of the intermediate solution during the reaction was analyzed via traditional bacterial growth. The specific experimental operation steps can be seen Text S2.

2.6. Theoretical computation

The theoretical calculations were performed via the Gaussian 16 suite of programs. The structures of the studied compounds were fully optimized at the M06-2X/def2-SVP level of theory. The vibrational frequencies of the optimized structures were carried out at the same level. The structures were characterized as a local energy minimum on the potential energy surface by verifying that all the vibrational frequencies were real. Wavefunction analysis was carried out with multi program, and two-dimensional valence-electron density color-filled maps of the two molecules were also given.

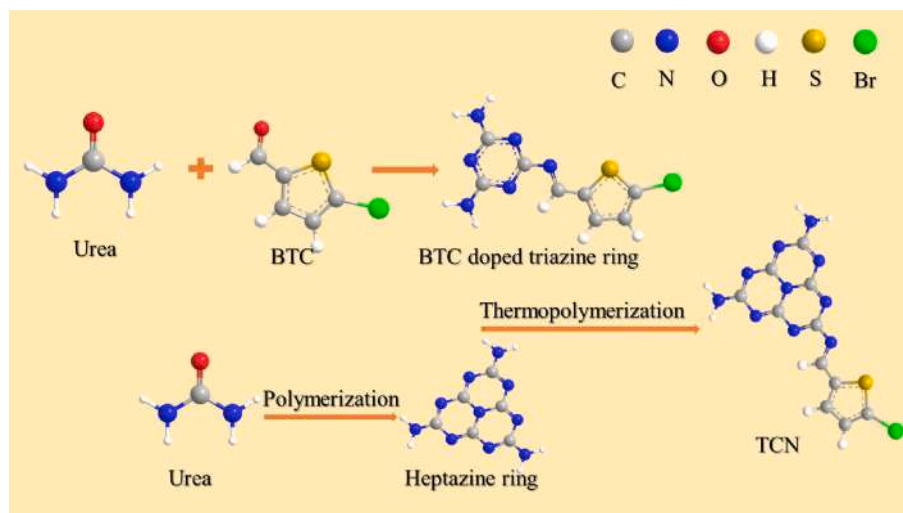
3. Results and discussion

3.1. Physicochemical properties

The $-\text{NH}_2$ group can promote the copolymerization between molecules [25,32,33]. As displayed in Scheme 1, in the presence of $-\text{NH}_2$ group, BTC incorporated CN was obtained through the copolymerization

of BTC and urea molecules. Thiophene and its derivatives are strong electron donors and Br is electron-withdrawing element [28-30]. The D-A type CN is composed of imine central core and Br atom as acceptor. By the bridging effect of imine, the π -electrons in thiophene tend to migrate to the heptazine rings in TCN. The TEM and SEM were employed to detect the morphologies of the TCN-5 and CN samples. The typical sheet-structured CN are exhibited in Fig. 1a and b. The nanosheets of TCN-5 become thinner and smaller compared to CN (Fig. 1c and d). The formation of smaller planes possibly ascribed to the hindered bonding degree of melon units during the polymerization process with BTC incorporation. Besides, N_2 adsorption-desorption isotherms was used to investigate the morphology changes. As displayed in Fig. S1a and b, CN and TCN-5 samples show similar mesopore distribution and type IV isotherm. The pore volume and BET specific surface area of TCN-5 are $0.422 \text{ cm}^3 \cdot \text{g}^{-1}$ and $85.157 \text{ m}^2 \cdot \text{g}^{-1}$, respectively, which are similar to those of CN ($0.401 \text{ cm}^3 \cdot \text{g}^{-1}$ and $86.934 \text{ m}^2 \cdot \text{g}^{-1}$), this shows that the internal microscopic changes of the two types of samples are not obvious.

Correspondingly, the four different samples (Fig. 2a) displayed similar peak patterns in the XRD patterns, the typical two peaks at 13° and 27.6° are attributed to the in-plane ordering of heptazine units and interlayer-stacking, respectively [27]. The grafted ones show lower and broader intensity probably due to the presence of disturbance in aromatic rings. In the Raman spectra of CN and TCN (Fig. 2b), the characteristic peaks at 985 and 705 cm^{-1} present the symmetric N-breathing mode and the in-plane bending of heptazine, while the characteristic peaks at 1150 – 1750 cm^{-1} correspond to the disordered graphitic C-N vibrations [27,34]. Moreover, Fig. 2c reflects the FTIR spectra of the investigated samples. Apparently, the modified samples show similar characteristic peaks compared to CN. Specifically, the peaks situated at 1100 – 1750 and 700 cm^{-1} correspond to aromatic C-N and heptazine rings and those at 3000 – 3300 cm^{-1} are characteristic signals of vibrational absorption of N-H group [11,27]. There are no other characteristic peaks, indicating that the doping amount of BTC is very small and does not change the basic structure of CN. In order to obtain more detailed structural features and chemical composition information, solid-state ^{13}C NMR test was then carried out. Two characteristic peaks at 150.5 ppm and 160.5 ppm can be indexed to the C_1 (CN_3) and C_2 ($\text{CN}_2(\text{NH}_x)$) carbons [17], can be seen in both samples in Fig. 2d. However, TCN-5 does not show a characteristic peak that is distinct from the CN sample. The doping amount of BTC in CN increased by 60 times was prepared for the purpose of better investing solid-state ^{13}C NMR spectrum. From Fig. 2e and f, an additional weak peak at 128.0 ppm ascribed to aromatic $\text{C}=\text{C}$ [17,25,34], which imply the successful



Scheme 1. Construction of D-A structured CN through copolymerization of BTC and urea.

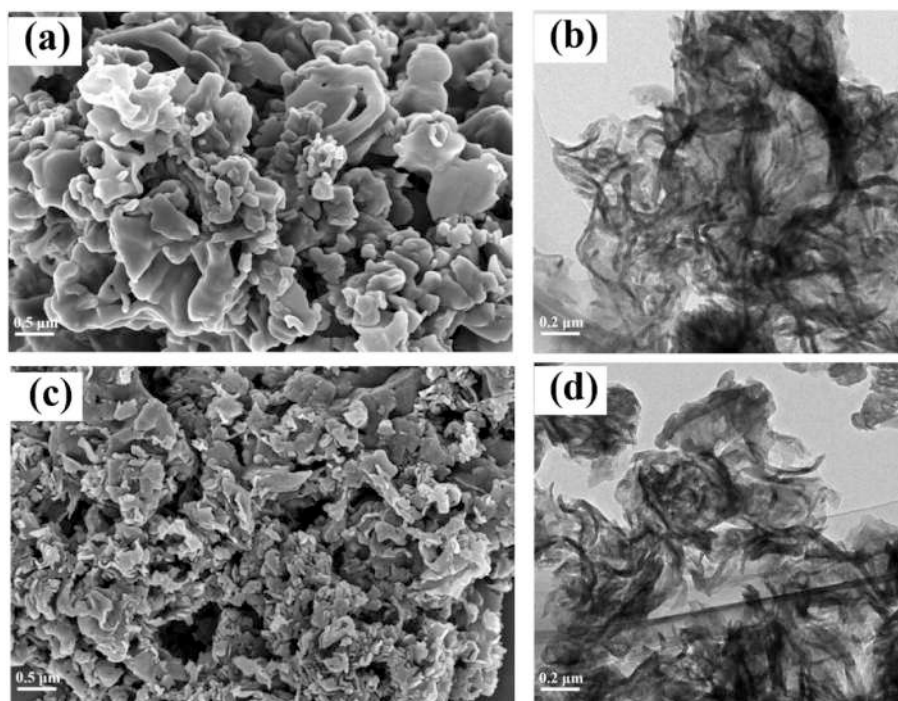


Fig. 1. SEM and TEM images of the (a and b) CN and (c and d) TCN-5.

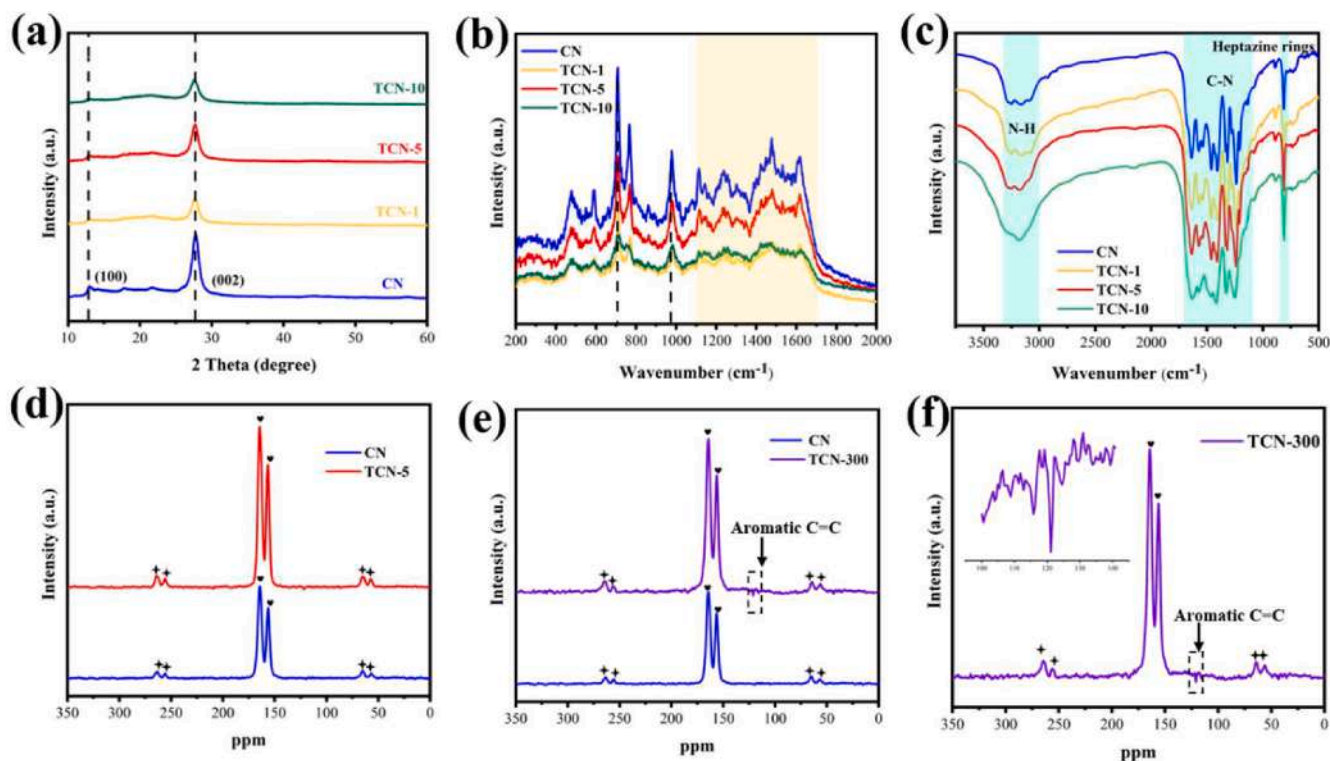


Fig. 2. (a) XRD patterns, (b) Raman spectra and (c) ATR-FTIR spectra of the samples; Solid-state ^{13}C NMR spectra of the (d) CN, (e and f) TCN-5 and TCN-300.

incorporation of the BTC moiety into the CN frameworks.

The XPS of the as-obtained CN, TCN-5 are exhibited in Fig. 3. The overall XPS survey spectrum almost shows no difference, this may be due to the insufficient amount of doping. In Fig. 3b, two distinct characteristic peaks locate at 284.81 and 288.34 eV, which belong to the aromatic C atoms and sp^2 hybridized C (N-C=N) from the heptazine ring, respectively. It is worth noting that the binding energies of N-C=N

in BTC (288.10 eV) are downgraded to a lower energy because of electron acquisition affect [32]. This phenomenon also occurs in the N 1s XPS spectra (Fig. 3c). The relatively stronger peak at 284.81 eV in TCN-5 is due to the presence of aromatic rings in BTC. For N 1s spectra (Fig. 3c), the samples show four peaks. The first peak at 398.65 eV belongs to the N atoms in C-N=C, the peak at 400.32 eV presents the N atoms from N-C₃. Besides, the other two peaks at 401.30 and 404.50 eV

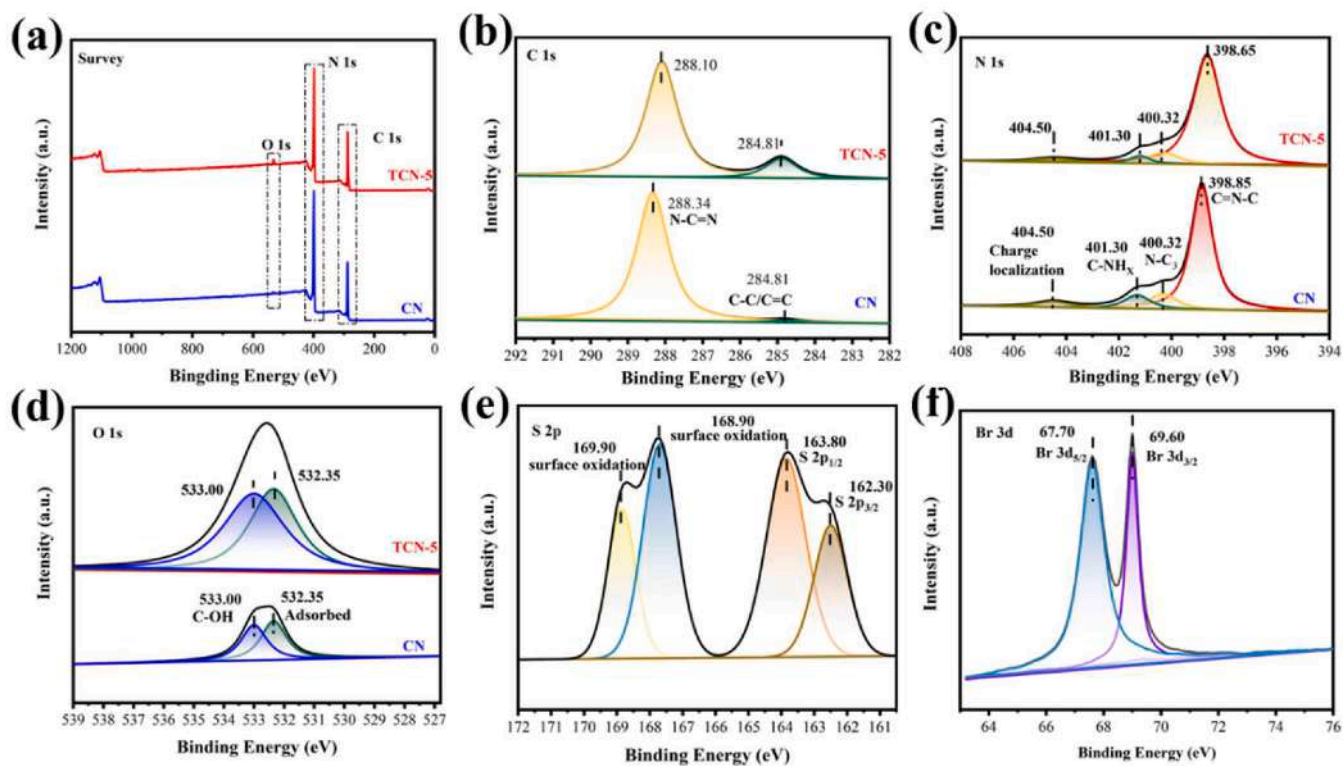


Fig. 3. XPS spectra of TCN-5 photocatalyst: (a) a survey spectrum; high-resolution spectra of (b) C 1s, (c) N 1s, (d) O 1s, (e) S 2p and (f) Br 3d.

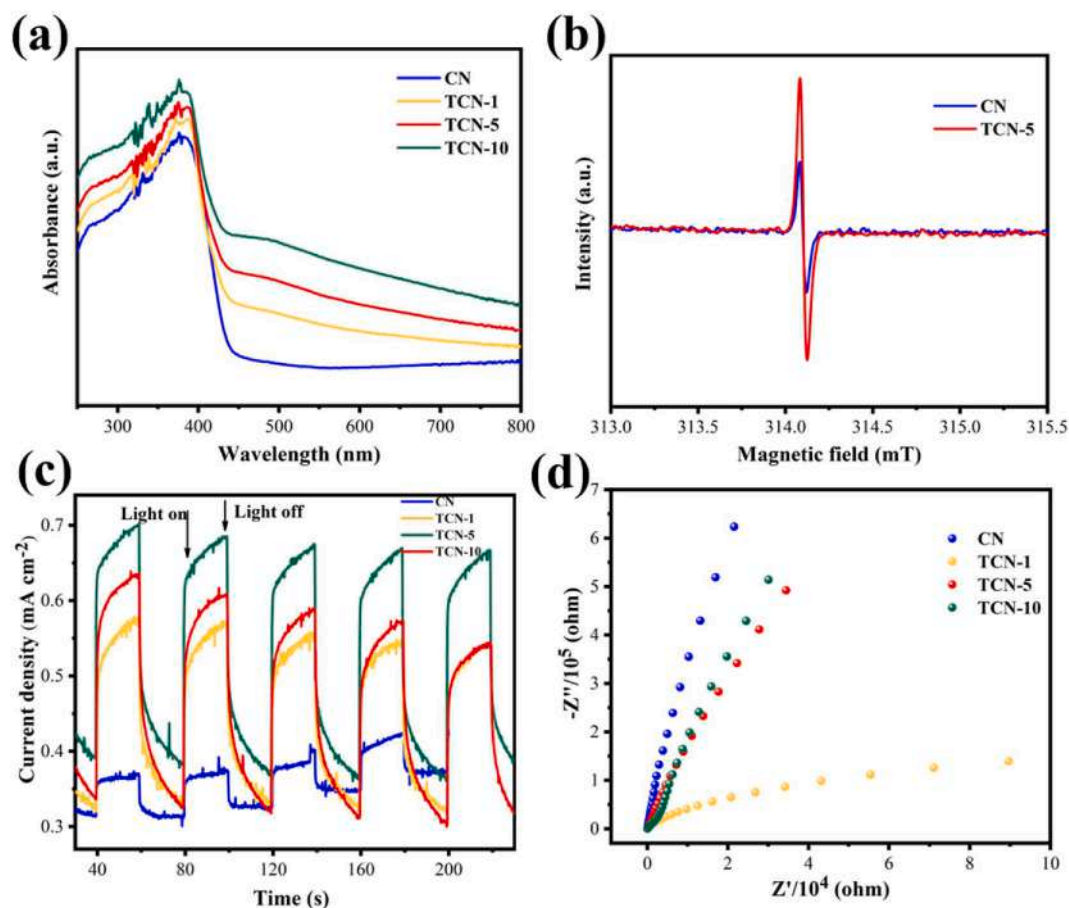


Fig. 4. (a) UV-vis diffusion reflection spectra; (b) EPR spectra; (c) transient photocurrent curves and (d) EIS of the samples.

are assigned to the binding energy of NH_x and the π -excitations charging effects [35]. Two peaks formed in the spectra of O 1s of the samples, with binding energies at around 533.00 and 532.35 eV, which assigned to O=C derived from urea or BTC and the adsorbed H_2O , respectively (Fig. 3d) [17,36]. It is noteworthy that the intensity of O=C in TCN-5 is higher than that in CN due to the existence of O=C bond in BTC. The S 2p spectra can be decomposed into four individual peaks at binding energy of 162.30 eV, 163.80 eV, 168.90 eV and 169.90 eV (Fig. 3e). The peaks located at 163.80 eV and 162.30 eV are associated with the $\text{S} 2\text{p}^{1/2}$ and $\text{S} 2\text{p}^{3/2}$ of S^{2-} , respectively. Besides, the surface oxidation formed two peaks at 168.90 and 169.90 eV during the surface oxidation occurred calcination [37]. Two characteristic peaks at around 67.70 and 69.60 eV are presented in Fig. 3f. The former presents Br $3\text{d}^{5/2}$ and the peak at 69.60 eV is ascribed to Br $3\text{d}^{3/2}$ [38]. Furthermore, the C/N atomic ratio in TCN-5 (0.81) was higher than that in CN (0.67) from the elemental analysis results (Table S1), which indicates that aromatic rings have been attached to the CN structure.

3.2. Optical and photoelectrochemical properties

The light absorption capacity is a key factor affecting the performance of the photocatalyst. UV/vis DRS of CN and TCN-5 are used to analyze the optical bandgap and light absorption capability. As displayed in Fig. 4a, CN exhibits a sharp light absorption edge at 450 nm. Nevertheless, the absorption edge of TCN is obviously redshifted and this trend is more obvious with the increase of BTC doping. From Fig. 4b, the electron paramagnetic resonance (EPR) showed a paramagnetic signal in the Lorentzian line shape at $g = 2.0032$ in both samples, implying the unpaired electrons are produced on the sp^2 C atoms from the π -conjugated aromatic ring [39].

Photocurrent response and EIS are tested to analyze the photoelectrochemical properties of the samples. As shown in Fig. 4c, in the experiment, the illumination time interval is 20 s. When visible light is irradiated on the sample, the photocurrent response phenomenon can be observed in all samples. All BTC-doped samples exhibit stronger photocurrent intensity than CN, the sample with the strongest

photocurrent density is TCN-5, followed by TCN-10 and TCN-1. Additionally, the electrical conductivity of the samples is displayed in Fig. 4d, CN shows the largest slope than TCN-10 and TCN-5 while TCN-1 has the smallest arc, which indicates that the electrical resistance of CN is larger than any other BTC-doped CN. Relatively smaller resistance means relatively greater conductivity, and greater conductivity will give the sample stronger electron transfer performance [39]. This result is roughly the same as the result of the photocurrent response experiment. All results show that it is easier to generate photo-excited electrons on the TCN, the separation and transfer of charges are more efficient on TCN.

To further investigate the properties of charge carrier recombination, other photoelectrochemical analysis including TRPL and PL techniques are conducted. From Fig. 5e, CN shows the PL curve of maximum density under 340 nm wavelength excitation condition. The curve densities of TCN gradually weak with BTC content increasing, which implies the accelerated charge separation and restricted charge recombination. The photogenerated charge carrier lifetimes of CN and TCN-5 were measured by the TRPL spectra, as shown in Fig. 5f. The average electron lifetimes are calculated by the following calculation method (Eq. (3)) and the calculation results can be seen in Table S2.

$$\tau_{ave} = \frac{B_1\tau_1 + B_2\tau_2}{B_1 + B_2} \quad (3)$$

τ_1 and τ_2 present the shorter and longer fluorescent lifetime, τ_{ave} is average electron lifetimes while B_1, B_2 are the corresponding normalized amplitudes. It can be known from the calculation results that the fluorescence lifetime of CN is 7.75 ns, which is greater than that of TCN-5 (5.96 ns). It is attributed to the donor-acceptor structure in CN, which promote the efficient intramolecular charge transfer [40].

The data of UV-vis DRS is applied to study the bandgap energy of the photocatalysts through the Kubelka-Munk function, as displayed in Fig. 5a. The bandgaps of CN, TCN-1, TCN-5 and TCN-10 are 2.67 eV, 2.26 eV, 2.22 eV and 1.90 eV, respectively. The narrowed band gap means that the TCN-5 can absorb more visible light than CN.

The Mott-Schottky curves of different samples with frequencies of

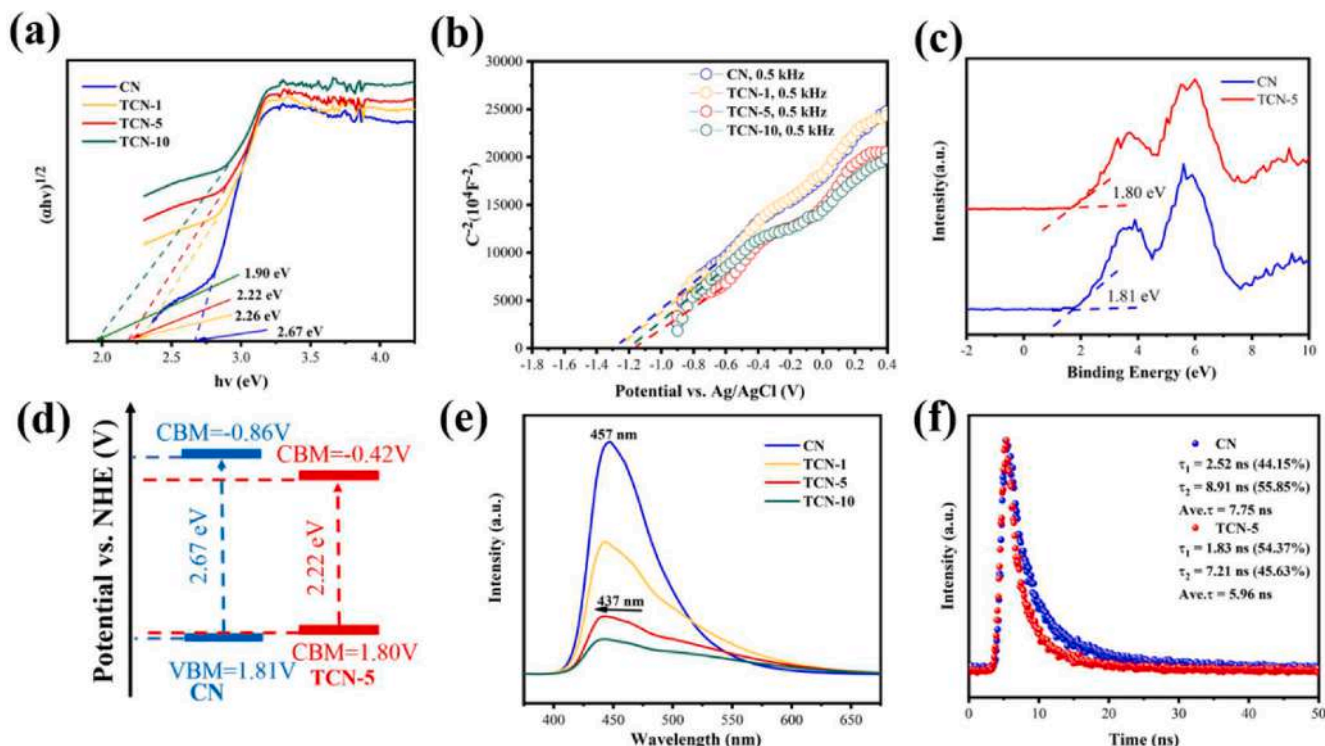


Fig. 5. (a) Tauc plots, (b) Mott-Schottky plot, (c) VB XPS spectra, (d) band structure diagrams, (e) steady-state PL spectra and (f) TRPL decay spectra of the samples.

500 Hz are shown in Fig. 5b, the slope drawn from the curve is positive, indicating that all the samples are n-type semiconductors [39]. The density of photogenerated carriers generated on each sample can be determined by the slope of the curve via the following formula (Eq. (4)):

$$ND = \frac{2}{q\epsilon\epsilon_0} \frac{1}{\text{slope}} \quad (4)$$

where q represents the amount of charge, ϵ and ϵ_0 represent the permittivity in vacuum and the dielectric constant of CN, and these three quantities are constants. Judging the carrier density and the slope of the curve according to the formula, it is not difficult to conclude that the charge carrier density of the TCN-5 sample is significantly higher than that of CN.

The band energy gap (E_g) of CN and TCN-5 are 2.67 and 2.22 eV respectively through calculation by the Kubelk-Munk function. Under visible light irradiation, more electrons are generated in TCN due to the narrowed band gap of TCN. Furthermore, the valence band (VB) potentials of CN and TCN-5 are 1.81 and 1.80 eV, which are obtained from the XPS valence band spectrum (Fig. 5c). Thus, the conduction band (CB) value can be estimated via the formula of $E_{CB} = E_{VB} - E_g$, where E_{VB} , E_{CB} and E_g present VB potential, CB potential and the band gap energy of the photocatalysts, respectively [39]. According to the calculation results, the CB potential of CN and TCN-5 are speculated to be -0.86 and -0.42 eV, respectively. And the band structure diagrams of both

samples can be seen in Fig. 5d.

3.3. Photocatalytic OTC degradation activities

3.3.1. Effect of catalytic behavior

This experiment takes OTC as the target pollutant, and studies the removal ability of different samples under visible light irradiation. All the catalytic systems undergo reactions under dark conditions for half an hour to reach the adsorption-desorption equilibrium between the OTC molecules and the photocatalysts. From Fig. 6a, in the system without photocatalyst, the concentration of OTC is basically unchanged, which indicates that the OTC is relatively stable and hardly decomposed. The degradation ability of each sample to OTC is different, which is in order of TCN-5 > TCN-10 > TCN-1 > CN > photolysis. Obviously, TCN-5 has the strongest ability to remove OTC under the same conditions, reaching 93.0%. When the doping amount of BTC exceeds 5 μL , the degradation ability decreases. This may be due to the excessive structural distortion leads to the formation of more electron and hole recombination sites. Moreover, the photocatalytic reaction kinetics of OTC is characterized by the apparent rate constant (k) via the following equation (Eq. (2)):

$$\ln C_t/C_0 = -k_1 t \quad (5)$$

The meanings of the letters are explained in section 2.4. As exhibited in the kinetic curves (Fig. 6b), the k value follows the order: TCN-5

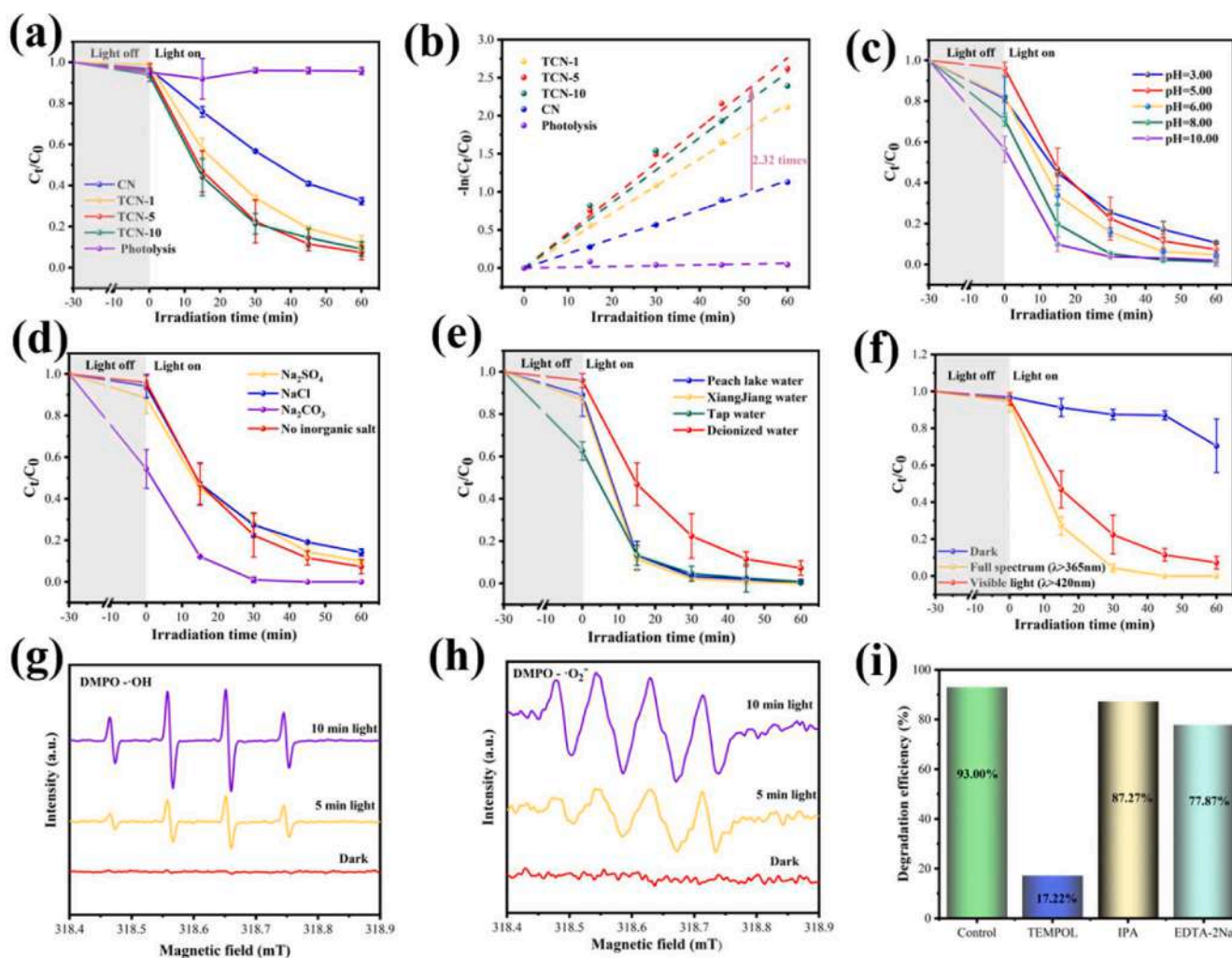


Fig. 6. (a) Photocatalytic degradation efficiency for OTC and (b) pseudo first-order kinetic fitting curves; effect of (c) pH; (d) inorganic salt; (e) different water samples and (f) different light irradiation conditions on the degradation of OTC over TCN-5 under visible light irradiation. ESR spectra of (g) DMPO-OH adduct and (h) DMPO-O₂⁻ adduct for the TCN-5, (i) photocatalytic degradation efficiency of OTC over the TCN-5 with different quenchers.

(0.04367 min^{-1}) > TCN-10 (0.0398 min^{-1}) > TCN-1 (0.0352 min^{-1}) > CN (0.0188 min^{-1}) > photolysis (0.0007 min^{-1}). The TCN-5 denotes the largest k value (0.04367 min^{-1}), which is 2.32 times than that of CN. The above results show that TCN-5 has the strongest ability for OTC removal. The OTC removal rate and rate constant k value of TCN-5 in TC and OTC degradation are significantly higher than those of other CN-based photocatalysts (Table S3, S4). In addition, TCN-5 also shows high degradation performance for other pollutants and a wide range of application (Fig.S2).

3.3.2. Effect of reaction pH

The pH of the reaction system is a key factor influencing the reaction process [41]. For the purpose of exploring the effect of pH on the photocatalytic process, the pH of the catalytic system was adjusted with dilute HNO_3 and NaOH solution. As displayed in Fig. 6c, when the pH of the system solution increases from 3.00 to 5.00, the photocatalytic activity increases, which shows that the acid will inhibit the reaction, because less $\cdot\text{OH}$ is generated under acidic conditions [10,41]. Because OTC is easy to self-decompose under alkaline environments [42], when the pH value of the system solution exceeds 5.00, OTC in the catalytic system will be easier to remove.

3.3.3. Effect of inorganic salts

The presence of inorganic coexisting salt ions in natural water body will affect the catalytic performance of the photocatalyst. In this work, three sodium salts (NaCl , Na_2SO_4 and Na_2CO_3) with the concentration of 0.05 M are adopted to explore the influence of different anions for practical applications (Fig. 6d). With the addition of other ions, the adsorption capacity of OTC by the catalyst decreases slightly because of promoted protonation by salt, causing electrostatic interaction between OTC ions and electrolyte ions to promote the dissociation of OTC molecules [43]. When SO_4^{2-} exists, the degradation of OTC is inhibited, because SO_4^{2-} is an efficient free radical scavenger, which can effectively capture the free radicals generated on the surface of photocatalyst [1,10,44]. The presence of CO_3^{2-} significantly accelerate the OTC removal. This may be because CO_3^{2-} can increase the pH value of the reaction system, which is conducive to the reaction [45]. It is observed that NaCl have a negligible effect on OTC removal. This is because the NaCl solution is neutral, and the addition of a small amount of NaCl does not change the environment of the reaction system, while Na^+ competes with OTC molecules for the catalytic site on the photocatalyst, resulting in the decline of OTC removal efficiency [1,44].

3.3.4. Effect of water sources

The actual water contains various ions, which will affect the practical application of photocatalyst. In order to explore its application in practical water bodies, we used several different locations as water source sampling points (Fig. S3) to explore the impact of water sources (Tap water, ultrapure water, Peach Lake water and Xiang Jiang water). The initial concentration of OTC is $20 \text{ mg}\cdot\text{L}^{-1}$, and the experimental results are displayed in Fig. 6e. The TCN-5 in deionized water has the strongest adsorption capacity for OTC. However, after the reaction, TCN-5 in deionized water shows a slightly weaker ability to remove OTC than in the other three systems. This is because the actual water body situation is more complicated, and the physical parameters and chemical composition are not the same, which affects the removal of OTC. Obviously, the TCN sample shows excellent removal ability in actual water bodies, which indicates that it has great potential in wastewater treatment.

3.3.5. Effect of light irradiation conditions

Solar light source will be the final and best energy choice for the operation of photocatalytic system [46]. The dark, full spectrum irradiation ($\lambda > 365 \text{ nm}$) and visible light irradiation condition ($\lambda > 420 \text{ nm}$) are selected for the influence of the light source elevation on the reaction. As shown in Fig. 6f, under dark conditions, the ability of TCN-5 for

OTC degradation is much weaker than that of visible light and full-spectrum illumination. Almost all the OTC can be removed after an hour full-spectrum irradiation. In addition, monochromatic irradiation experiments are performed to explore the influence of the wavelength on the photochemical response. The photocatalytic degradation of OTC is carried out under the illumination of monochromatic light with four different wavelengths of 399 nm, 448 nm, 497 nm and 550 nm, respectively. Fig. S4 shows the OTC removal efficiency under the monochromatic light with four different wavelengths, using the TCN-5 sample as the photocatalyst. The result indicates that the photocatalytic efficiency of TCN-5 is closely related to the irradiation wavelength, the xenon lamp with shorter wavelengths is more effective for OTC photodegradation. This phenomenon can be attributed to that the shorter the wavelength of light, the higher the corresponding photon vibration frequency and the greater the energy of photons [46-48]. This will be conducive to the generation and separation of photogenerated carriers and promote the reaction. The wavelength-dependent OTC removal efficiency in the optimum TCN-5 sample is determined to be about 80% at 399 nm and retain about 20% at 550 nm. The photocatalytic activity of CN for removing OTC is lower than that of TCN-5 under the irradiation of four monochromatic lights.

3.3.6. Photocatalyst stability tests

The stability and recyclability of photocatalyst determine its practical application. Therefore, we have conducted three cycle tests on TCN-5, the results are shown in Fig. Fig. S6a. After three cycles for OTC removal, the photocatalytic performance of photocatalyst does not change significantly, only decreased by about 10%, still higher than 80%. Furthermore, it can be seen from the XRD, FTIR spectra and Raman spectra patterns of the sample, the chemical and crystal structure of the samples after multiple reactions have hardly changed (Fig. S5, Fig. S6b-d). The above results show that TCN-5 has a good recyclability and chemical stability, and it will be very promising in the field of photocatalytic removal of pollutants.

3.4. Reactive species identification

The active species take a critical role in the OTC degradation process, several reactive species trapping experiments were used to verify the main active species generated in reaction. The EDTA-2Na, TEMPOL and IPA were used as quencher of h^+ , $\cdot\text{OH}$ and $\cdot\text{O}_2^-$, respectively. As presented in Fig. 6i, when the TEMPOL is present in the system solution, the photocatalytic removal efficiency of OTC is significantly reduced, and the removal efficiency is greatly reduced to 17.22%, indicating that $\cdot\text{O}_2^-$ is a crucial active substance for OTC degradation. When EDTA-2Na is added into reaction system, the degradation efficiency is about 15% lower than when no trapping material is added. Moreover, when IPA presents in the reaction system, the degradation removal efficiency of OTC does not change significantly. It demonstrated that h^+ also has a great removal effect on OTC, while $\cdot\text{OH}$ is basically ineffective. Besides, ESR technology was applied to further affirm the above-mentioned active species ($\cdot\text{OH}$ and $\cdot\text{O}_2^-$) generated in OTC degradation process. As exhibited in Fig. 6g and h, in dark conditions, no signal peak is generated, with the emergence of irradiation, a characteristic signal peak appears, and the intensity of the peak gradually increases with the extension of radiation time. The 1:2:2:1 and 1:1:1:1 density signals correspond to $\text{DMPO}\cdot\text{OH}$ and $\text{DMPO}\cdot\text{O}_2^-$ [9], respectively. The above results indicate $\cdot\text{O}_2^-$ and h^+ play dominant role in the degradation reaction, while $\cdot\text{OH}$ acts as an assistant derived from H_2O_2 decomposing [49].

3.5. Possible degradation pathway of OTC

In the progress of photocatalytic reaction, a series of intermediates will be produced. Combined with the data from LC-MS/MS, the photocatalytic mechanism and related previous works [12,50], it can be

inferred that OTC undergoes series of reactions such as dehydration, deamination, deamidation, de-hydroxylation and demethylation [51,52], then be gradually degraded. The possible degradation paths of OTC are shown in the Fig. S7 and the intermediates produced in the reaction is listed in Fig. S8 and Table S5, including their structure, m/z and molecular formula. OTC initially produced intermediate OTC 1 ($m/z = 443.1$) through dehydration. The product OTC 7 ($m/z = 429.0$) is formed by loss N-methyl group of OTC1, then OTC 8 ($m/z = 419.0$) is produced from OTC 7 via ring-opening reaction. In the second degradation path, OTC is converted into OTC 2 ($m/z = 383.0$) by the dehydration process, de-hydroxylation and deamidation. And due to hydroxylation and loss N-methyl groups, OTC 2 is degraded to OTC 4 ($m/z = 372.2$). Then OTC 4 is further degraded into OTC 5 ($m/z = 279.1$) through fragmentation, which undergo de-hydroxylation reaction in the next step to generate OTC 6 ($m/z = 262.9$). Moreover, OTC 3 undergoes the same degradation path as OTC 2 and be finally converted into the same product. In the end, both OTC 6 and OTC 8 are further decomposed to produce substances with smaller molecular weights, such as OTC 9 ($m/z = 104.0$), OTC 10 ($m/z = 165.0$), OTC 11 ($m/z = 114.0$) and OTC 12 ($m/z = 180.0$). After more degradation steps, these small molecules will eventually degrade into CO_2 and H_2O .

Above all the results and discussions, the possible photocatalytic OTC degradation mechanism over TCN-5 is exhibited in Scheme 2. Thiophene is strong electron donor and can also act as a chromophoric center to harvest photons [28,53-55], which supplies more excitons and facilitates the electron transfer to CN when irradiated by visible light. When irradiated by visible light, photo-generated electrons and holes are generated on TCN-5 (Eq. (5)). On account of the existence of the D-A structure in the photocatalyst, the π electrons in the thiophene structure tend to transfer to the heptazine ring in the TCN through the imine bond. On the other hand, CN can also transfer its photogenerated holes to the electron donor molecule and hence suppress the significant recombination of holes and electrons. At the same time, the π electron cloud will also be competitively shifted to the Br atom due to the electronegativity induction effect of the Br atom. The standard redox potential of $\text{O}_2/\cdot\text{O}_2^-$ (-0.33 V vs. NHE) is more positive than the CB of TCN-5 (-0.42 V vs. NHE), which indicates that the accumulated electrons can reduce O_2 to $\cdot\text{O}_2^-$ (Eq. (6)) [39]. Next, the $\cdot\text{O}_2^-$ can further react with the electrons and H^+ to form H_2O_2 , followed by the formation of $\cdot\text{OH}$ (Eq. (7) and (8)) [39,49]. Subsequently, The produced h^+ , $\cdot\text{O}_2^-$, and $\cdot\text{OH}$ act as important active species for OTC degradation (Eq. (9)). Moreover, to understand the delicate changes of electronic migration, theoretical calculations of electron density are performed. As shown in Fig. S9, the state of

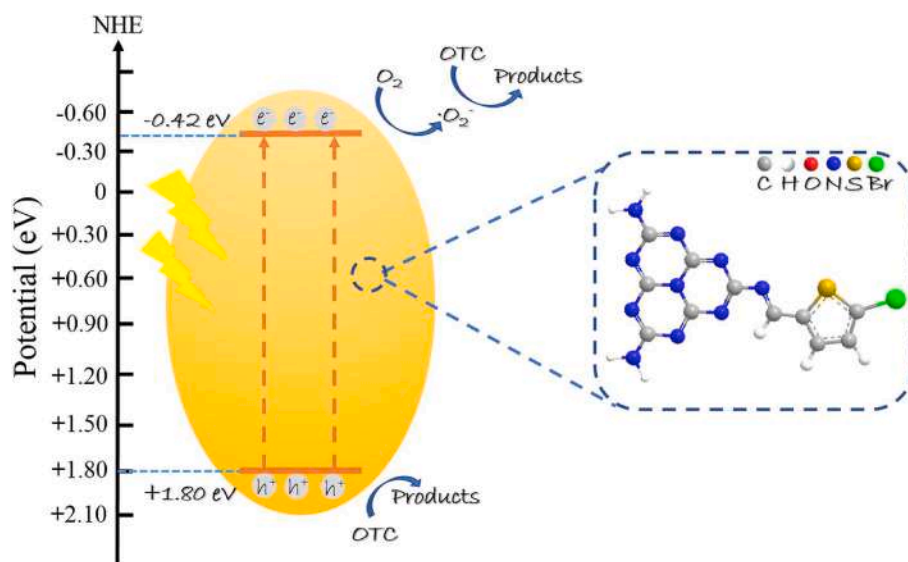
electronic configuration for the CN and TCN-5 are revealed by the two-dimensional valence-electron density color-filled maps. The density is the highest in the Br atoms of TCN-5, indicating the strongest electron-withdrawing properties. The thiophene as an electron donor has the lowest electron intensity. Meanwhile, the charge density of C atoms and N atoms in TCN-5 are lower than that in CN, which may be due to the uneven charge distribution induced by the electronic migration. Thus, the electronic migration-induced uneven polarity between the heptazine rings, imine linkage and Br atoms to form continuous intramolecular charge transfer to accelerate electron-hole separation.



3.6. Toxicity analysis

Generally, substances with large molecular weight undergo many steps to achieve degradation, and some intermediates or by-products produced during the degradation process may be more toxic than the parent substance [41]. Therefore, it is of great significance to effectively estimate the toxicity of degradation intermediates. In our experiment, the growth and survival of the gram-negative strain *E. coli* are used to verdict the toxicity of the reaction solution. As shown in Fig. S10, the growth inhibition rate of OTC solution on *E. coli* reaches >50%, and inhibition rate of bacterial growth shows a downward trend with reaction time prolonging. This shows that the intermediate products produced by OTC degradation are less toxic than OTC and are beneficial for *E. coli* growth. Normally, the toxic effect on bacteria is negatively related to the degree of mineralization of pollutants. As the reaction progresses, the ratio of $\text{TOC}_t/\text{TOC}_0$ decline with the continuous removal of OTC (Fig. S10b). At the end of the reaction (at 60 min), the removal efficiency of TOC and OTC are 38.0% and 93.0%. The above results indicate that the use of TCN-5 photocatalytic technology to remove OTC is very environmental friendly.

Other assessment parameters such as bioaccumulation factor, mutagenicity, oral rat LD50 and the LC50 of fathead minnow are



Scheme 2. The possible photocatalytic degradation mechanism of OTC over TCN-5.

measured to further evaluate the toxicity of degradation intermediates based on the T.E.S.T [51,56-58]. The results are exhibited in Fig. S11. A total of ten reaction intermediates including OTC are elevated (Table S3). As shown in Fig. S11a, the bioaccumulation factors of almost all the intermediates are higher than that OTC except for product B, C and E, meaning that these by-products are easier to accumulate in organisms than OTC. From Fig. S11b, the LD50 rat values for half of OTC products are higher than that of OTC, indicating that these intermediates are less toxic, probably because they are more mineralized. OTC has a “mutagenicity positive” and most of the products still show “mutagenicity positive” after reaction (Fig. S11c), implying that it is difficult to change mutagenicity. In addition, the LC50 value of fathead minnow are all higher than OTC (Fig. S11d), meaning low toxicity of the generated products.

4. Conclusions

In summary, we successfully constructed a D-A system based on CN for boosting the photocatalytic performance via copolymerization effect between BTC and urea, followed by thermal oxidation in air. Benefitting from the intramolecular charge transfer formation, the force-directed migration of electrons in TCN was realized, thus leading to the improved electronic and optical performance. As results, in the case of the optimized samples (TCN-5) under visible light irradiation, 93.0% of OTC can be removed and the mineralization rate reaches 38.0%. The photocatalytic rate constant of TCN-5 is significantly improved by about 2.32 times compared to pristine CN. And the intermediates are less toxic, probably because they are more mineralized. This work further deepens the exploration of the intramolecular charge transfer in the CN molecules and provides new inspiration for the design of high-performance polymeric CN based photocatalysts for organic pollutants degradation.

Declaration of Competing Interest

The authors declare that they have no known competing financial interests or personal relationships that could have appeared to influence the work reported in this paper.

Acknowledgments

This study was financially supported by the program for the National Natural Science Foundation of China (52170162, 51809090, 52170161), Innovation Program of Hunan Province (2021RC3049, 2020RC3025), the Natural Science Foundation of Hunan Province (2019JJ50077, 2020JJ3009), and the Fundamental Research Funds for the Central Universities (531118010114).

Appendix A. Supplementary data

Supplementary data to this article can be found online at <https://doi.org/10.1016/j.cej.2022.137370>.

References

- Y. Yang, Z. Zeng, C. Zhang, D. Huang, G. Zeng, R. Xiao, C. Lai, C. Zhou, H. Guo, W. Xue, M. Cheng, W. Wang, J. Wang, Construction of iodine vacancy-rich BiOI/Ag@AgI Z-scheme heterojunction photocatalysts for visible-light-driven tetracycline degradation: transformation pathways and mechanism insight, *Chem. Eng. J.* 349 (2018) 808–821, <https://doi.org/10.1016/j.cej.2018.05.093>.
- F. Qin, J. Li, C. Zhang, G. Zeng, D. Huang, X. Tan, D. Qin, H. Tan, Biochar in the 21st century: a data-driven visualization of collaboration, frontier identification, and future trend, 151774 151774, *Sci. Total Environ.* (2021), <https://doi.org/10.1016/j.scitotenv.2021.151774>.
- H. Tan, J. Li, M. He, J. Li, D. Zhi, F. Qin, C. Zhang, Global evolution of research on green energy and environmental technologies: a bibliometric study, *J. Environ. Manage.* 297 (2021), 113382, <https://doi.org/10.1016/j.jenvman.2021.113382>.
- C. Huang, C. Zhang, D. Huang, D. Wang, S. Tian, R. Wang, Y. Yang, W. Wang, F. Qin, Influence of surface functionalities of pyrogenic carbonaceous materials on the generation of reactive species towards organic contaminants: a review, *Chem. Eng. J.* 404 (2021), 127066, <https://doi.org/10.1016/j.cej.2020.127066>.
- C. Zhang, S. Tian, F. Qin, Y. Yu, D. Huang, A. Duan, C. Zhou, Y. Yang, W. Wang, Y. Zhou, H. Luo, Catalyst-free activation of permanganate under visible light irradiation for sulfamethazine degradation: Experiments and theoretical calculation, *Water Res.* 194 (2021) 116915, <https://doi.org/10.1016/j.watres.2021.116915>.
- S. Tian, C. Zhang, D. Huang, R. Wang, G. Zeng, M. Yan, W. Xiong, C. Zhou, M. Cheng, W. Xue, Y. Yang, W. Wang, Recent progress in sustainable technologies for adsorptive and reactive removal of sulfonamides, *Chem. Eng. J.* 389 (2020), 123423, <https://doi.org/10.1016/j.cej.2019.123423>.
- C. Zhang, C. Lai, G. Zeng, D. Huang, C. Yang, Y. Wang, Y. Zhou, M. Cheng, Efficacy of carbonaceous nanocomposites for sorbing ionizable antibiotic sulfamethazine from aqueous solution, *Water Res.* 95 (2016) 103–112, <https://doi.org/10.1016/j.watres.2016.03.014>.
- L. Qin, Z. Wang, Y. Fu, C. Lai, X. Liu, B. Li, S. Liu, H. Yi, L. Li, M. Zhang, Z. Li, W. Cao, Q. Niu, Gold nanoparticles-modified MnFe₂O₄ with synergistic catalysis for photo-Fenton degradation of tetracycline under neutral pH, *J. Hazard. Mater.* 414 (2021), 125448, <https://doi.org/10.1016/j.jhazmat.2021.125448>.
- G. Fang, J. Li, C. Zhang, F. Qin, H. Luo, C. Huang, D. Qin, Z. Ouyang, Periodate activated by manganese oxide/biochar composites for antibiotic degradation in aqueous system: combined effects of active manganese species and biochar, *Environ. Pollut.* 300 (2022) 118939.
- C. Zhang, D. He, S. Fu, G. Zeng, Q. Liang, Y. Yang, D. Huang, W. Wang, Y. Zhou, Silver iodide decorated ZnSn(OH)₆ hollow cube: room-temperature preparation and application for highly efficient photocatalytic oxytetracycline degradation, *Chem. Eng. J.* 421 (2021), 129810, <https://doi.org/10.1016/j.cej.2021.129810>.
- Y. Yang, C. Zhang, D. Huang, G. Zeng, J. Huang, C. Lai, C. Zhou, W. Wang, H. Guo, W. Xue, R. Deng, M. Cheng, W. Xiong, Boron nitride quantum dots decorated ultrathin porous g-C₃N₄: intensified exciton dissociation and charge transfer for promoting visible-light-driven molecular oxygen activation, *Appl. Catal., B* 245 (2019) 87–99, <https://doi.org/10.1016/j.apcatb.2018.12.049>.
- X. He, H. Shang, C. Wang, L. Chen, Z. Gong, J. Wang, S. Zhao, J. Ma, Significantly influenced photocatalytic performance for H₂O₂ generation over ultrathin g-C₃N₄ through regulating the migration orientation of photogenerated charge carriers, *Chin. Chem. Lett.* 32 (11) (2021) 3377–3381, <https://doi.org/10.1016/j.ccl.2021.04.028>.
- Y. Yang, G. Zeng, D. Huang, C. Zhang, D. He, C. Zhou, W. Wang, W. Xiong, B. Song, H. Yi, S. Ye, X. Ren, In situ grown single-atom cobalt on polymeric carbon nitride with bidentate ligand for efficient photocatalytic degradation of refractory antibiotics, *Small* 16 (29) (2020), 200163, <https://doi.org/10.1002/sml.202001634>.
- A. Li, Q. Cao, G. Zhou, B.V.K.J. Schmidt, W. Zhu, X. Yuan, H. Huo, J. Gong, M. Antonietti, Three-phase photocatalysis for the enhanced selectivity and activity of CO₂ reduction on a hydrophobic surface, *Angew. Chem.-Int. Edit.* 58 (41) (2019) 14549–14555, <https://doi.org/10.1002/anie.201908058>.
- D. Qin, Y. Zhou, W. Wang, C. Zhang, G. Zeng, D. Huang, L. Wang, H. Wang, Y. Yang, L. Lei, S. Chen, D. He, Recent advances in two-dimensional nanomaterials for photocatalytic reduction of CO₂: insights into performance, theories and perspective, *J. Mater. Chem. A* 8 (37) (2020) 19156–19195, <https://doi.org/10.1039/d0ta07460h>.
- D. Huang, X. Sun, Y. Liu, H. Ji, W. Liu, C.-C. Wang, W. Ma, Z. Cai, A carbon-rich g-C₃N₄ with promoted charge separation for highly efficient photocatalytic degradation of amoxicillin, *Chin. Chem. Lett.* 32 (9) (2021) 2787–2791, <https://doi.org/10.1016/j.ccl.2021.01.012>.
- Z. Sun, Y. Jiang, L. Zeng, L. Huang, Intramolecular charge transfer and extended conjugate effects in donor-acceptor-type mesoporous carbon nitride for photocatalytic hydrogen evolution, *ChemSusChem* 12 (7) (2019) 1325–1333, <https://doi.org/10.1002/cssc.201802890>.
- C. Zhou, Z. Zeng, G. Zeng, D. Huang, R. Xiao, M. Cheng, C. Zhang, W. Xiong, C. Lai, Y. Yang, W. Wang, H. Yi, B. Li, Visible-light-driven photocatalytic degradation of sulfamethazine by surface engineering of carbon nitride: properties, degradation pathway and mechanisms, *J. Hazard. Mater.* 380 (2019), 120815, <https://doi.org/10.1016/j.jhazmat.2019.120815>.
- M.-Y. Ye, Z.-H. Zhao, Z.-F. Hu, L.-Q. Liu, H.-M. Ji, Z.-R. Shen, T.-Y. Ma, OD/2D heterojunctions of vanadate quantum dots/graphitic carbon nitride nanosheets for enhanced visible-light-driven photocatalysis, *Angew. Chem.-Int. Edit.* 56 (29) (2017) 8407–8411, <https://doi.org/10.1002/anie.201611127>.
- Y. Wang, X. Liu, J. Liu, B. Han, X. Hu, F. Yang, Z. Xu, Y. Li, S. Jia, Z. Li, Y. Zhao, Carbon quantum dot implanted graphite carbon nitride nanotubes: excellent charge separation and enhanced photocatalytic hydrogen evolution, *Angew. Chem.-Int. Edit.* 57 (20) (2018) 5765–5771, <https://doi.org/10.1002/anie.201802014>.
- Y. Zhou, C. Zhang, D. Huang, W. Wang, Y. Zhai, Q. Liang, Y. Yang, S. Tian, H. Luo, D. Qin, Structure defined 2D Mo₂C/2Dg-C₃N₄ Van der Waals heterojunction: oriented charge flow in-plane and separation within the interface to collectively promote photocatalytic degradation of pharmaceutical and personal care products, *Appl. Catal., B* 301 (2022) 120749, <https://doi.org/10.1016/j.apcatb.2021.120749>.
- A. Hayat, N. Shaishta, S.K.B. Mane, J. Khan, A. Hayat, Rational ionothermal copolymerization of TCNQ with PCN semiconductor for enhanced photocatalytic full water splitting, *ACS Appl. Mater. Interfaces* 11 (50) (2019) 46756–46766, <https://doi.org/10.1021/acsami.9b15537>.
- H. Che, C. Liu, G. Che, G. Liao, H. Dong, C. Li, N. Song, C. Li, Facile construction of porous intramolecular g-C₃N₄-based donor-acceptor conjugated copolymers as

- highly efficient photocatalysts for superior H₂ evolution, *Nano Energy* 67 (2020), 104273, <https://doi.org/10.1016/j.nanoen.2019.104273>.
- [24] K. Li, W.-D. Zhang, Creating graphitic carbon nitride based donor-pi-acceptor-pi-donor structured catalysts for highly photocatalytic hydrogen evolution, *Small* 14 (12) (2018) 1703599, <https://doi.org/10.1002/smll.201703599>.
- [25] C. Zhu, T. Wei, Y. Wei, L. Wang, M. Lu, Y. Yuan, L. Yin, L. Huang, Unravelling intramolecular charge transfer in donor-acceptor structured g-C₃N₄ for superior photocatalytic hydrogen evolution, *J. Mater. Chem. A* 9 (2) (2021) 1207–1212, <https://doi.org/10.1039/d0ta08609f>.
- [26] C. Zhou, G. Zeng, D. Huang, Y. Luo, M. Cheng, Y. Liu, W. Xiong, Y. Yang, B. Song, W. Wang, B. Shao, Z. Li, Distorted polymeric carbon nitride via carriers transfer bridges with superior photocatalytic activity for organic pollutants oxidation and hydrogen production under visible light, *J. Hazard. Mater.* 386 (2020), 121947, <https://doi.org/10.1016/j.jhazmat.2019.121947>.
- [27] Y. Yang, G. Zeng, D. Huang, C. Zhang, D. He, C. Zhou, W. Wang, W. Xiong, X. Li, B. Li, W. Dong, Y. Zhou, Molecular engineering of polymeric carbon nitride for highly efficient photocatalytic oxytetracycline degradation and H₂O₂ production, *Appl. Catal., B* 272 (2020) 118970. <https://doi.org/10.1016/j.apcatb.2020.118970>.
- [28] Y. Chen, J. Zhang, M. Zhang, X. Wang, Molecular and textural engineering of conjugated carbon nitride catalysts for selective oxidation of alcohols with visible light, *Chem. Sci.* 4 (8) (2013) 3244–3248, <https://doi.org/10.1039/c3sc51203g>.
- [29] J.M. Notestein, E. Iglesia, A. Katz, Photoluminescence and charge-transfer complexes of calixarenes grafted on TiO₂ nanoparticles, *Chem. Mater.* 19 (20) (2007) 4998–5005, <https://doi.org/10.1021/cm070779c>.
- [30] R.G. George, M. Padmanabhan, Studies on some new meso-aryl substituted octabromo-porphyrins and their Zn(II) derivatives, *Polyhedron* 22 (23) (2003) 3145–3154, <https://doi.org/10.1016/j.poly.2003.07.001>.
- [31] J. Lu, T. Wang, Y. Zhou, C. Cui, Z. Ao, Y. Zhou, Dramatic enhancement effects of l-cysteine on the degradation of sulfadiazine in Fe³⁺/CaO₂ system, *J. Hazard. Mater.* 383 (2020), 121133, <https://doi.org/10.1016/j.jhazmat.2019.121133>.
- [32] Z. Sun, Y. Jiang, L. Zeng, X. Zhang, S. Hu, L. Huang, Controllable local electronic migration induced charge separation and red-shift emission in carbon nitride for enhanced photocatalysis and potential phototherapy, *Chem. Commun.* 55 (43) (2019) 6002–6005, <https://doi.org/10.1039/c9cc02749a>.
- [33] X. Fan, L. Zhang, R. Cheng, M. Wang, M. Li, Y. Zhou, J. Shi, Construction of graphitic C₃N₄-based intramolecular donor – acceptor conjugated copolymers for photocatalytic hydrogen evolution, *ACS Catal.* 5 (9) (2015) 5008–5015, <https://doi.org/10.1021/acscatal.5b01155>.
- [34] J. Kroeger, A. Jimenez-Solano, G. Savasci, P. Rovo, I. Moudrakovski, K. Kuester, H. Schlomberg, H.A. Vignolo-Gonzalez, V. Duppel, L. Grunenberg, C.B. Dayan, M. Sitti, F. Podjaski, C. Ochsensfeld, B.V. Lotsch, Interfacial engineering for improved photocatalysis in a charge storing 2D carbon nitride: melamine functionalized poly(heptazine imide), *Adv. Energy Mater.* 11 (6) (2021) 2003016, <https://doi.org/10.1002/aenm.202003016>.
- [35] C. Zhou, D. Huang, P. Xu, G. Zeng, J. Huang, T. Shi, C. Lai, C. Zhang, M. Cheng, Y. Lu, A. Duan, W. Xiong, M. Zhou, Efficient visible light driven degradation of sulfamethazine and tetracycline by salicylic acid modified polymeric carbon nitride via charge transfer, *Chem. Eng. J.* 370 (2019) 1077–1086, <https://doi.org/10.1016/j.cej.2019.03.279>.
- [36] D.K.L. Chan, J.C. Yu, Facile synthesis of carbon- and oxygen-rich graphitic carbon nitride with enhanced visible-light photocatalytic activity, *Catal. Today* 310 (2018) 26–31, <https://doi.org/10.1016/j.cattod.2017.05.017>.
- [37] Y. Yue, P. Zhang, W. Wang, Y. Cai, F. Tan, X. Wang, X. Qiao, P.K. Wong, Enhanced dark adsorption and visible-light-driven photocatalytic properties of narrower-band-gap Cu₂S decorated Cu₂O nanocomposites for efficient removal of organic pollutants, *J. Hazard. Mater.* 384 (2020), 121302, <https://doi.org/10.1016/j.jhazmat.2019.121302>.
- [38] W. Zhao, W. Wang, H. Shi, 2D/2D Z-scheme BiO_{1-x}Br/g-C₃N₄ heterojunction with rich oxygen vacancies as electron mediator for enhanced visible-light degradation activity, *Appl. Surf. Sci.* 528 (2020), 146925, <https://doi.org/10.1016/j.apsusc.2020.146925>.
- [39] C. Zhang, D. Qin, Y. Zhou, F. Qin, H. Wang, W. Wang, Y. Yang, G. Zeng, Dual optimization approach to Mo single atom dispersed g-C₃N₄ photocatalyst: morphology and defect evolution, *Appl. Catal. B* 303 (2022) 120904.
- [40] B. Li, H. Song, F. Han, L. Wei, Photocatalytic oxidative desulfurization and denitrogenation for fuels in ambient air over Ti₃C₂/g-C₃N₄ composites under visible light irradiation, *Appl. Catal., B* 269 (2020) 118845. <https://doi.org/10.1016/j.apcatb.2020.118845>.
- [41] Z. Ouyang, Y. Yang, C. Zhang, S. Zhu, L. Qin, W. Wang, D. He, Y. Zhou, H. Luo, F. Qin, Recent advances in photocatalytic degradation of plastics and plastic-derived chemicals, *J. Mater. Chem. A* 9 (23) (2021) 13402–13441, <https://doi.org/10.1039/d0ta12465f>.
- [42] J. Han, S.P. Hu, Y. Wang, J.J. Ma, Extraction of oxytetracycline hydrochloride in aqueous two-phase system of acetone and ammonium sulfate, *J. Chem. Soc. Pak.* 35 (1) (2013) 11–16.
- [43] X. Tan, Y. Liu, Y. Gu, S. Liu, G. Zeng, X. Cai, X. Hu, H. Wang, S. Liu, L. Jiang, Biochar pyrolyzed from MgAl-layered double hydroxides pre-coated ramie biomass (*Boehmeria nivea* (L.) Gaud.): Characterization and application for crystal violet removal, *J. Environ. Manage.* 184 (2016) 85–93, <https://doi.org/10.1016/j.jenvman.2016.08.070>.
- [44] B. Li, C. Lai, G. Zeng, L. Qin, H. Yi, D. Huang, C. Zhou, X. Liu, M. Cheng, P. Xu, C. Zhang, F. Huang, S. Liu, Facile hydrothermal synthesis of Z-scheme Bi₂Fe₄O₉/Bi₂WO₆ heterojunction photocatalyst with enhanced visible light photocatalytic activity, *ACS Appl. Mater. Interfaces* 10 (22) (2018) 18824–18836, <https://doi.org/10.1021/acsami.8b06128>.
- [45] J.H.O.S. Pereira, V.J.P. Vilar, M.T. Borges, O. Gonzalez, S. Esplugas, R.A. R. Boaventura, Photocatalytic degradation of oxytetracycline using TiO₂ under natural and simulated solar radiation, *Sol. Energy* 85 (11) (2011) 2732–2740, <https://doi.org/10.1016/j.solener.2011.08.012>.
- [46] B. Zhou, X.u. Zhao, H. Liu, J. Qu, C.P. Huang, Visible-light sensitive cobalt-doped BiVO₄ (Co-BiVO₄) photocatalytic composites for the degradation of methylene blue dye in dilute aqueous solutions, *Appl. Catal. B* 99 (1–2) (2010) 214–221.
- [47] Y. Sang, H. Liu, A. Umar, Photocatalysis from UV/Vis to near-infrared light: towards full solar-light spectrum activity, *ChemCatChem* 7 (4) (2015) 559–573, <https://doi.org/10.1002/cctc.201402812>.
- [48] H. Zhou, S. Xu, D. Zhang, S. Chen, J. Deng, One step in situ synthesis of core-shell structured Cr₂O₃:P/fibrous-phosphorus hybrid composites with highly efficient full-spectrum-response photocatalytic activities, *Nanoscale* 9 (9) (2017) 3196–3205, <https://doi.org/10.1039/c6nr09584d>.
- [49] Y. Wang, F. He, L. Chen, J. Shang, J. Wang, S. Wang, H. Song, J. Zhang, C. Zhao, S. Wang, H. Sun, Acidification and bubble template derived porous g-C₃N₄ for efficient photodegradation and hydrogen evolution, *Chin. Chem. Lett.* 31 (10) (2020) 2668–2672, <https://doi.org/10.1016/j.ccl.2020.08.003>.
- [50] W. Wang, Q. Niu, G. Zeng, C. Zhang, D. Huang, B. Shao, C. Zhou, Y. Yang, Y. Liu, H. Guo, W. Xiong, L. Lei, S. Liu, H. Yi, S. Chen, X. Tang, 1D porous tubular g-C₃N₄ capture black phosphorus quantum dots as 1D/0D metal-free photocatalysts for oxytetracycline hydrochloride degradation and hexavalent chromium reduction, *Appl. Catal., B* 273 (2020) 119051. <https://doi.org/10.1016/j.apcatb.2020.119051>.
- [51] H. Ji, P. Du, D. Zhao, S. Li, F. Sun, E.C. Duin, W. Liu, 2D/1D graphitic carbon nitride/titanate nanotubes heterostructure for efficient photocatalysis of sulfamethazine under solar light: Catalytic “hot spots” at the rutile-anatase-titanate interfaces, *Appl. Catal., B* 263 (2020) 118357. <https://doi.org/10.1016/j.apcatb.2019.118357>.
- [52] W. Qi, J. Long, C. Feng, Y. Feng, D. Cheng, Y. Liu, J. Xue, Z. Li, Fe³⁺ enhanced degradation of oxytetracycline in water by pseudomonas, *Water Res.* 160 (2019) 361–370, <https://doi.org/10.1016/j.watres.2019.05.058>.
- [53] J. Meng, Y. Tian, C. Li, X. Lin, Z. Wang, L. Sun, Y. Zhou, J. Li, N. Yang, Y. Zong, F. Li, Y. Cao, H. Song, A thiophene-modified double-shell hollow g-C₃N₄ nanosphere boosts NADH regeneration via synergistic enhancement of charge excitation and separation, *Catal. Sci. Technol.* 9 (8) (2019) 1911–1921, <https://doi.org/10.1039/c9cy00180h>.
- [54] J. Zhang, M. Zhang, S. Lin, X. Fu, X. Wang, Molecular doping of carbon nitride photocatalysts with tunable bandgap and enhanced activity, *J. Catal.* 310 (2014) 24–30, <https://doi.org/10.1016/j.jcat.2013.01.008>.
- [55] F. Ge, S. Huang, J. Yan, L. Jing, F. Chen, M. Xie, Y. Xu, H. Xu, H. Li, Sulfur promoted n-π* electron transitions in thiophene-doped g-C₃N₄ for enhanced photocatalytic activity, *Chin. J. Catal.* 42 (3) (2021) 450–459, [https://doi.org/10.1016/s1872-2067\(20\)63674-9](https://doi.org/10.1016/s1872-2067(20)63674-9).
- [56] S. Tang, Z. Wang, D. Yuan, C. Zhang, Y. Rao, Z. Wang, K. Yin, Ferrous ion-tartaric acid chelation promoted calcium peroxide fenton-like reactions for simulated organic wastewater treatment, *J. Clean Prod.* 268 (2020), 122253, <https://doi.org/10.1016/j.jclepro.2020.122253>.
- [57] J. Jiang, X. Wang, Y. Liu, Y. Ma, T. Li, Y. Lin, T. Xie, S. Dong, Photo-Fenton degradation of emerging pollutants over Fe-POM nanoparticle/porous and ultrathin g-C₃N₄ nanosheet with rich nitrogen defect: Degradation mechanism, pathways, and products toxicity assessment, *Appl. Catal., B* 278 (2020) 119349. <https://doi.org/10.1016/j.apcatb.2020.119349>.
- [58] M. Dou, J. Wang, B. Gao, C. Xu, F. Yang, Photocatalytic difference of amoxicillin and cefotaxime under visible light by mesoporous g-C₃N₄: mechanism, degradation pathway and DFT calculation, *Chem. Eng. J.* 383 (2020), 123134, <https://doi.org/10.1016/j.cej.2019.123134>.